JOURNAL OF GEOPHYSICAL RESEARCH, VOL. 114, B08310, doi:10.1029/2008JB006085, 2009

Denoising seismic noise cross correlations

A. M. Baig,[1] M. Campillo,[1] and F. Brenguier[2]

Received 9 September 2008; revised 18 March 2009; accepted 18 June 2009; published 29 August 2009.

[1] Seismic noise cross correlations have become a novel way of probing the elastic structure of the Earth without relying on an often highly nonuniform and sporadic distribution of earthquakes. By circumventing this restriction, one can determine the elastic Green's function between any two points where instruments exist. For tomography, this will allow for a larger distribution of crossing paths and therefore better resolution in the inversions. One can also monitor the same station pair Green's functions for changes in the state of the Earth, an application that has been employed in volcanic monitoring. One limitation of this cross-correlation technique is that the input time series are frequently very long to recover high-fidelity signals. We present two time-frequency stacking algorithms to denoise the correlated signals and to alleviate this problem; increasing signal-to-noise ratios allows for high-fidelity Green's functions to be constructed from shorter time series. We demonstrate the increase in signal fidelity by applying these routines to seismic data, first to ambient noise across southern California and then to data from le Piton de la Fournaise volcano on La Réunion Island. In the former, we find that denoising the data allows for more traveltimes to be measured, particularly at longer station separations, across all passbands examined except for long-period Love waves, where no data are recovered. In the latter, we apply a time-frequency denoising algorithm to resolve subtle shifts in phase in cross correlations between seismic stations that occur before eruptions: we see a clear precursor to the June 2000 eruption.

Citation: Baig, A. M., M. Campillo, and F. Brenguier (2009), Denoising seismic noise cross correlations, *J. Geophys. Res.*, *114*, B08310, doi:10.1029/2008JB006085.

1. Introduction

[2] The theoretical result that cross correlations of seismic noise are proportional to the elastic Green's function between the two stations [e.g., *Lobkis and Weaver*, 2001; *Shapiro and Campillo*, 2004; *Gouédard et al.*, 2008] has a wide variety of applications. Practically, however, a very long time signal of noise is required to produce coherent identifiable signals. Potentially, more stations pairs could be used in this cross-correlation tomography approach if more signals could be identified on the reconstructed Green's functions. The cross correlation of noise has been used also for monitoring of temporal changes of seismic velocities [*Wegler et al.*, 2006; *Nishimura et al.*, 2005; *Brenguier et al.*, 2008b, 2008a]. In this field of application too, enhancing the signal-to-noise ratio is required to obtain more precise measurements.

[3] To significantly boost the signal-to-noise ratios we develop a couple algorithms based on the time-to-time-frequency S transform [*Stockwell et al.*, 1996] and the discrete orthonormal S transform introduced by *Stockwell* [2007]. This first of these algorithms is a modified version of the time-frequency stacking algorithm presented by *Pinnegar and Eaton* [2003] and is designed to enhance surface wave phases. Fundamental mode Rayleigh and Love waves have been observed in correlations of seismic noise between stations hundreds and even thousands of kilometers apart [*Shapiro and Campillo*, 2004]. The dispersion of these waves has even been used to construct seismic tomographic images of the crust and upper mantle [*Shapiro et al.*, 2005; *Sabra et al.*, 2005; *Moschetti et al.*, 2007; *Stehly et al.*, 2009]. Unlike more conventional surface wave tomography, using observations of earthquakes, these noise correlations offer the opportunity for a much higher degree of resolution. Because earthquakes are far from evenly distributed, it can be challenging to have enough crossing raypaths in more traditional tomography to avoid smearing of anomalous structure. By contrast, the distribution of raypaths in these noise correlation studies depends only on the distribution of stations, which is very even over several regions. A study taking advantage of the density of stations in California demonstrated this point: by taking advantage of the increased density introduced into the state by USArray, *Shapiro et al.* [2005] produced images of crustal seismic velocity structure with a resolution of between 60 and 100 km, roughly the average interstation distance. We apply our denoising algorithm to USArray data from southern California. From those data, we measure traveltimes from both the denoised and unprocessed data in

[1] Laboratoire de Géophysique Interne et de Tectonophysique, Grenoble, France.
[2] Institut de Physique du Globe de Paris, Paris, France.

0148-0227/09/2008JB006085$09.00

several passbands. We compare the number of data that we are able to extract from each data set to determine how effect our denoising routine is.

[4] We use a slightly different filter, building on the ideas of phase coherence [*Schimmel and Paulssen*, 1997; *Schimmel and Gallart*, 2007], for an application where we are interested in the coherence of the coda of these noise cross correlations. By measuring subtle changes of traveltime in the coda of the cross correlations, *Brenguier et al.* [2008b] detected changing properties in the medium prior to volcanic eruptions. We construct a data adaptive filter based on the day-to-day coherence of arrivals in the coda of the noise cross correlations for each station pair and then apply that filter to the data in order to improve the robustness of the estimates of subtle traveltime changes.

2. S Transform

[5] The S transform [*Stockwell et al.*, 1996] decomposes data from the time domain, $x(t)$, and projects it into a highly redundant time-frequency (τ, f) domain:

$$S(\tau,f) = \frac{1}{\sqrt{2\pi}} \int_{\infty}^{\infty} x(t)|f| \exp\left[-\frac{(\tau - t)^2 f^2}{2} - i2\pi ft\right] dt. \quad (1)$$

For the discretized $x(kT)$, at sampling interval T over N points with the usual discrete Fourier transform $X(n/NT)$ (k and n are the time and frequency samples, respectively), the S transform is written after a little manipulation as

$$S\left(jT, \frac{n}{NT}\right) = \sum_{m=0}^{N-1} X\left(\frac{m+n}{NT}\right) \exp\left[-2\pi^2 \frac{m^2}{n^2} - i2\pi \frac{mj}{N}\right] \quad (2)$$

for $n \neq 0$ and

$$S(jT, 0) = \frac{1}{N} \sum_{m=0}^{N-1} x\left(\frac{m}{NT}\right) \quad (3)$$

for $n = 0$. The inverse S transform is realized by, for each frequency, summing over each time sample in and then performing an inverse Fourier transform:

$$x(kT) = \sum_{n=0}^{N-1} \left[\frac{1}{N} \sum_{j=0}^{N-1} S\left(jT, \frac{n}{NT}\right)\right] \exp\left(i2\pi \frac{nk}{N}\right). \quad (4)$$

Though the S transform provides a powerful tool for analyzing signals, it is redundant in that an N point signal is represented by N^2 points in the time-frequency plane making the transformation somewhat inefficient.

[6] A recent development, the discrete orthogonal S transform (DOST) [*Stockwell*, 2007], has solved this problem in an approach reminiscent of wavelet analysis. An N point signal is projected onto N basis vectors, and each basis vector maps onto a patch of time-frequency space. These orthonormal basis functions are both highly localized in time and compactly supported in frequency. For a particular sampling of time-frequency space (described by *Stockwell* [2007] as octave sampling) the basis functions are described as

$$S_{[p,\tau]}(jT) = \frac{ie^{-i\pi\tau}}{\sqrt{N}2^{(p-1)/4}} \cdot \frac{\exp\left[-i2\pi h\left(2^{(p-1)} - \frac{1}{2}\right)\right] - \exp\left[-i2\pi h\left(2^{p} - \frac{1}{2}\right)\right]}{2\sin(\pi h)} \quad (5)$$

for $h = \frac{j}{N} - \frac{\tau}{2(p-1)} \neq 0$ and

$$S_{[p,\tau]}(jT) = -\frac{2^{(p-1)/4}}{\sqrt{N}} \exp(i\pi\tau), h = 0, \quad (6)$$

where p is the octave number ranging from 2 to $\log_2(N) - 1$, and τ is a temporal index variable that ranges between 0 and $2(p-1) - 1$ for each octave. For $p = 0$, $S_{[0,0]}(jT) = 1/\sqrt{N}$, for p = 1,

$$S_{[1,0]}(jT) = \frac{1}{\sqrt{N}} \exp\left(-\frac{i2\pi j}{N}\right), \quad (7)$$

and we need one basis function for the Nyquist frequency

$$S_{[\mathrm{Nyq}]}(jT) = \frac{1}{\sqrt{N}} \exp(i\pi j). \quad (8)$$

For a signal, $x(t)$, the time-frequency representation, $X(p, \tau)$, is formed by projecting the data onto the DOST basis functions:

$$X(p,\tau) = x(t) S_{[p,\tau]}(jT), \quad (9)$$

and the inverse transform is performed by projecting $X(p, \tau)$ onto the complex conjugates of the same basis functions:

$$x(t) = X(p,\tau) S^*_{[p,\tau]}(jT). \quad (10)$$

Figure 1 shows four examples of DOST basis functions for different values of $[p, \tau]$: for each function both the real (solid line) and imaginary (dash-dotted line) parts are plotted along with their amplitude envelopes (dotted line). The plotted functions are over two different octaves and are adjacent in time index, τ. The envelopes reveal that the time localization of these functions is fairly good and that they are compactly supported in the frequency domain. It is worth noting that the function themselves are not self-similar which distinguishes them from wavelets. This lack of self-similarity allows for the entire suite of these basis functions to be orthogonal, however, which gives the benefit of being extremely easy to manipulate.

[7] These two time-frequency representations discussed above are shown together with a synthetic surface wave seismogram in Figure 2. The synthetic (Figure 2, top) is the vertical component of a receiver 500 km away from an explosive source at the surface of a two layer over a half-space model. Therefore, the largest arrival on the seismogram is that of a fundamental mode Rayleigh wave. The absolute value of the fully redundant S transform (Figure 2, middle)

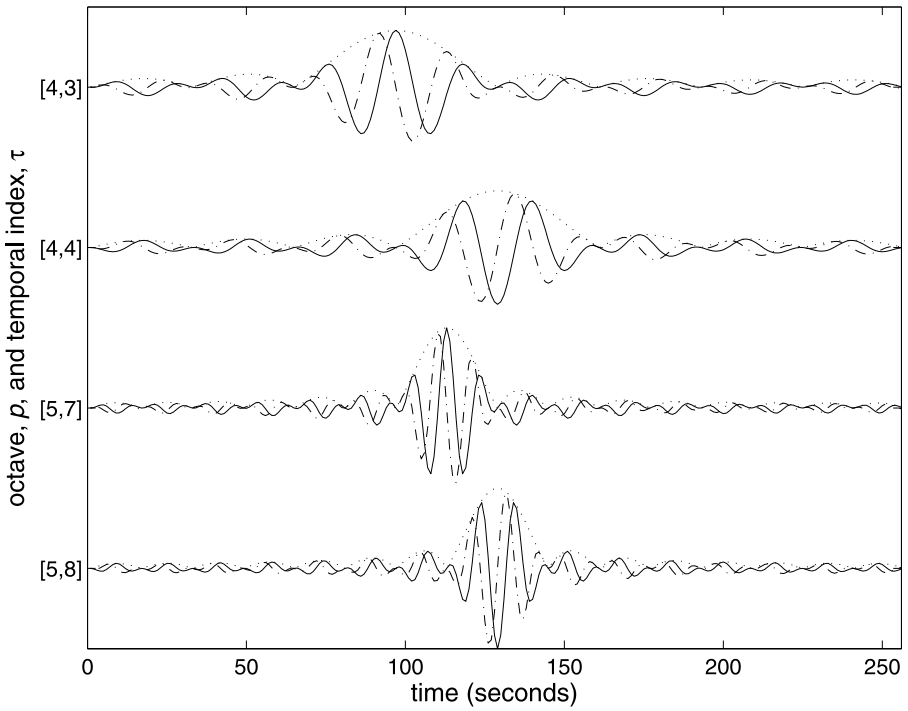

Figure 1. Real (solid line) and imaginary (dot-dashed line) parts together with the amplitude envelope (dotted line) for four basis functions for the discrete orthonormal S transform.

shows the dispersive nature of this arrival well. The colors range from blue, representing zero amplitude to the highest amplitudes in red. There is some energy, in light blue, at frequencies above the main arrival: these represent higher-mode Rayleigh waves. We also project each of the N DOST basis vector on the N point synthetic seismogram. The absolute value of each projection (Figure 2, bottom) is assigned to the patch of time-frequency space represented by its basis vector. In this way, we obtain a figure that appears like a "blockier" version of the fully redundant S transform (Figure 2, middle). However, this blockiness is a manifestation of the realities of simultaneous resolution of time and frequency. The poorly spectrally localized basis vectors at the highest frequencies are much better localized in time than the basis vectors for the lowest frequencies, though these latter vectors have much better frequency resolution. We note that the overall features of the fully redundant S transform are still present in this realization of the signal and that there is energy where the higher modes appear in the signal.

3. Stacking and Denoising With the DOST

[8] In order to generate a noise cross correlation, typically each component, x_m, of particle displacement, $x_m(\mathbf{r}_i, t)$, from each station, i, at location $\mathbf{r}_i$ is divided into N_k smaller segments (i.e., months, days, hours). Each segment is then cross-correlated with each component, x_n, from another station, $x_n(\mathbf{r}_j, t)$, then all the cross correlations are stacked. So the stacked cross correlation $C_{mn}(\mathbf{r}_i, \mathbf{r}_j, t)$, would be formed as

$$C_{mn}(\mathbf{r}_i, \mathbf{r}_j, t) = \sum_{k=1}^{N_k} \int_{t_k}^{t_{k+1}} x_m(\mathbf{r}_i, s) x_n(\mathbf{r}_j, t+s)\, ds. \qquad (11)$$

For the three components of the particle displacement at station i cross-correlated with each of the three components at station j, and assuming the recorded noise is being excited from all azimuths, [*Campillo and Paul*, 2003; *Sabra et al.*, 2005] show this signal will be related to the nine-component elastic Green's function of the Earth between the two stations, $G_{mn}(\mathbf{r}_i, \mathbf{r}_j, t)$, by

$$\dot{C}_{mn}(\mathbf{r}_i, \mathbf{r}_j, t) = b\left[G_{mn}(\mathbf{r}_i, \mathbf{r}_j, t) - G_{mn}(\mathbf{r}_i, \mathbf{r}_j, -t)\right], \qquad (12)$$

where the dot denotes differentiation with respect to time and $b < 0$ is a negative constant of proportionality.

[9] To further enhance the signals beyond stacking, we present two algorithms based on the DOST. We determine the patches of time-frequency space that are the most coherent across the signal, and then use that information to design a time-frequency filter to dampen the incoherent signals. The advantage of using a time-frequency representation, in contrast to more traditional purely spectral filters, is that it allows for noise in the same passband as the signal can be excluded from the signal so long as it is temporally separated from the arrivals that we wish to emphasize.

3.1. Relative Amplitude Filter

[10] To improve signal-to-noise ratios, we use the DOST to produce a data adaptive filter for each cross correlation. This procedure is based on a method presented by *Pinnegar and Eaton* [2003] where they used the fully redundant S transform; we use the DOST basis functions to economize computing time. After the shorter segments of the signal are cross-correlated, the stack of the absolute values of each

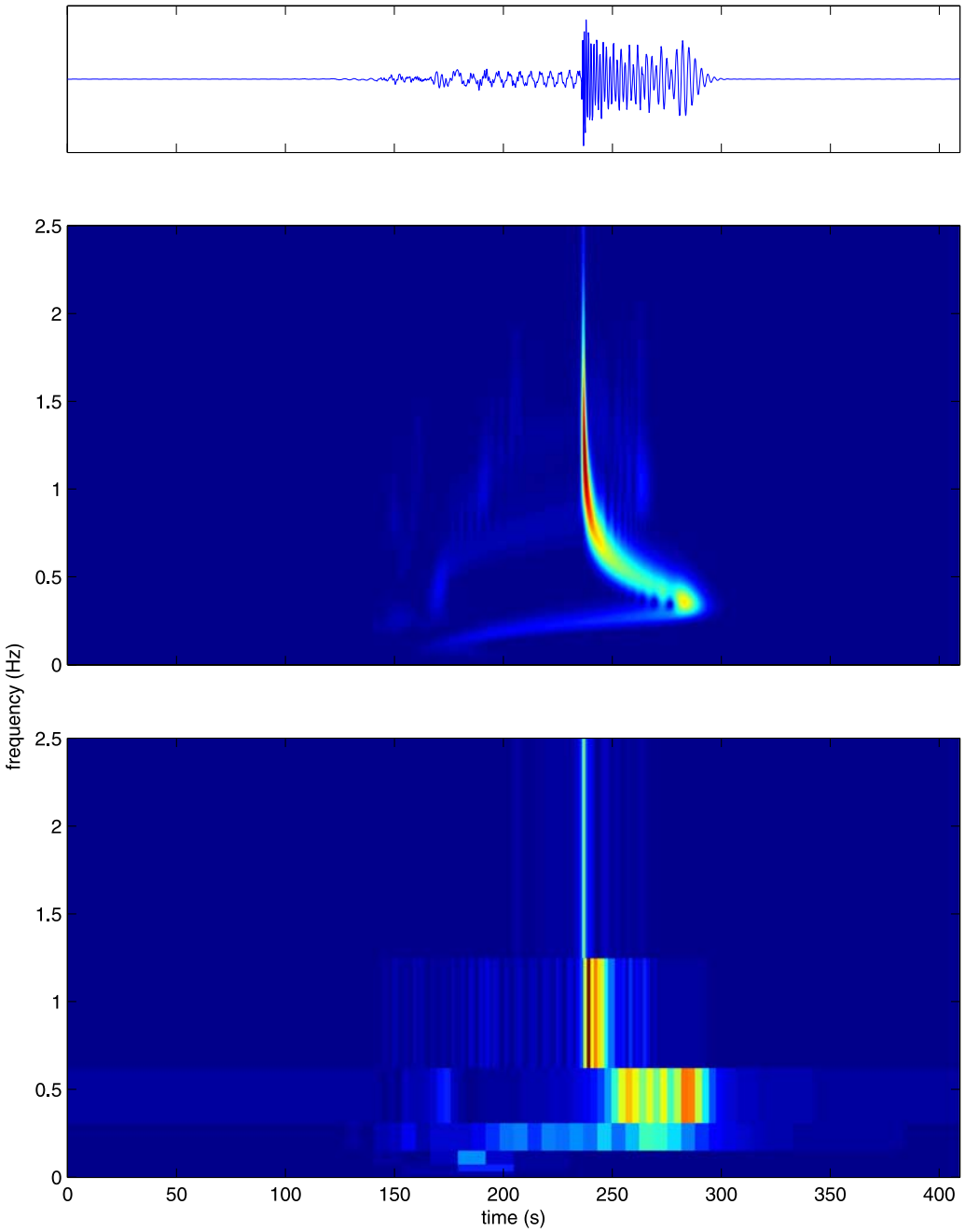

Figure 2. (top) A synthetic seismogram showing a Rayleigh wave; (middle) the absolute value of the S transform of the synthetic; and (bottom) the absolute value of the coefficients of DOST basis vectors for the synthetic with each number coefficient plotted at its appropriate patch of time-frequency space.

projection of the DOST basis vectors form a time-frequency representation of that signal:

$$w(p,\tau) = \sum_{k=1}^{N_k} \left| \int S_{[p,\tau]}(t) c_k(t), dt \right| \tag{13}$$

where $c_k(t)$ is one component of the cross-correlation tensor for day k and the spatial dependence has been dropped for convenience. We can then use this stack, $w(p, \tau)$, to define a filter such that it ranges between zero and one, and passes those parts of the signal that are the most coherent in time-frequency space. We rescale the stack in such a way that over each octave, p, (except the lowest octaves with the poorest temporal resolution), and both the causal and anticausal parts of the signal, the coefficients of the filter $f_A(p, \tau)$ will range between zero and one. Furthermore, in each window we smooth the normalized coefficients to minimize possible Gibb's phenomena by treating each window of coefficients as a time series, applying a narrow band pass filter, and taking the envelope. So, for each octave, p, we subdivide the range of τ in two (to treat the

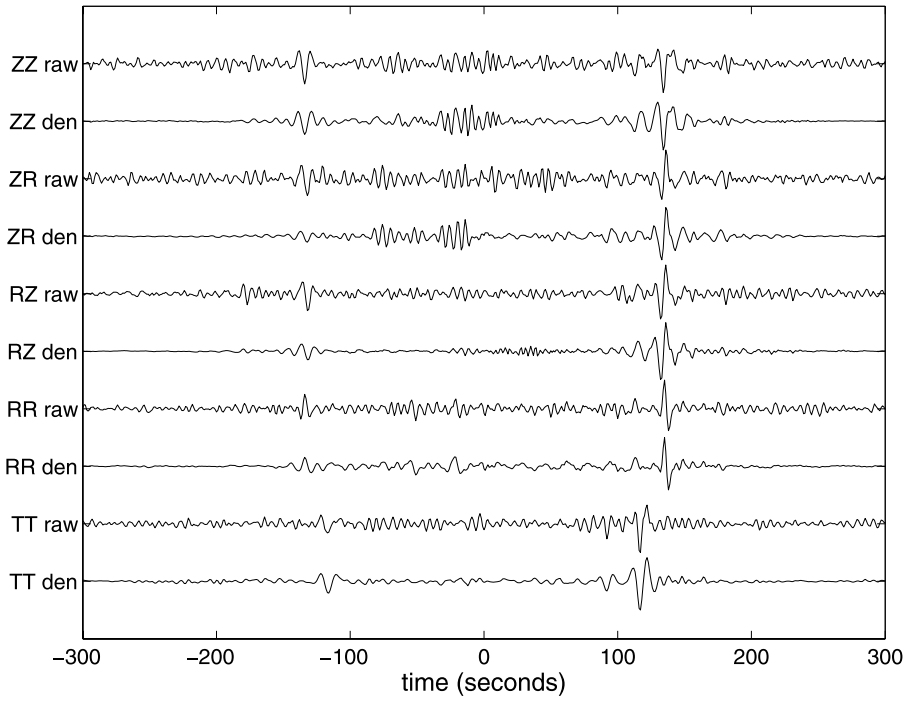

Figure 3. Stacked, unfiltered noise−cross correlation plotted alternately with the data after denoising has been applied. The data represent all five considered cross components between stations GLA and LRL.

causal and acausal parts of the signal independently) and define the filter over this range as

$$f_A(p,\tau) = \text{smoothed}\left\{\frac{w(p,\tau) - \min[w(p,\tau)]}{\max[w(p,\tau) - \min[w(p,\tau)]]}\right\}^{\nu}, \quad (14)$$

where the parameter, ν, may be used to control the strength of the filter. In practice, we find $\nu = 2$ achieves a balance of filtering away the incoherent arrivals while avoiding Gibb's phenomena. Because this filter emphasizes those signals that have the highest amplitudes in the correlations for a given octave, p, we shall call this filter the relative amplitude filter. By treating the two halves of the signal separately, we do not exacerbate any asymmetry already present in the cross correlation [*Stehly et al.*, 2006]. This filter is then applied to the stack of cross correlations, $C(t)$, by decomposing the signal into its DOST basis functions, weighting the coefficients by $f_A(p, \tau)$, and then transforming back to the time domain:

$$\tilde{C}(t) = \sum_{p,\tau} \left[f_A(p,\tau) S_{[p,\tau]}(t) C(t)\right] S^*_{[p,\tau]}(t). \quad (15)$$

In Figure 3, we compare cross correlations obtained through conventional stacking with one obtained through using relative amplitude filters on these stacks. The denoised data (denoted by the abbreviation, "den") generally have higher signal-to-noise rations than the unfiltered data (denoted by "raw") and the fundamental mode surface wave appears in the data with much less distortion surrounding it. The time-frequency filter used for the ZZ cross components in Figure 3 is shown in Figure 4. Although there is marked asymmetry in the filter, due to the persistent generation of 5−10 s period Rayleigh waves from the tidal interaction of the Pacific Ocean on the California coast [*Stehly et al.*, 2006], the dispersive nature of the cross correlation is evident in the fact that (especially for positive time) the peaks of the filter shift further back in frequency. The time-frequency construction of the denoising algorithm is evident upon comparing the processed and unprocessed traces: noise in the same band has been eliminated in the denoised traces (e.g., comparing Rayleigh wave cross components at −170 s) due to its incoherence. However, the relative amplitude filter sometimes preserves some of the acausal energy around zero time in the traces. This energy could be a limitation in the assumption that the noise is isotropically distributed: some coherent noise arrives from the coast obliquely with respect to the station geometry and appears near zero time in the cross correlations.

3.2. Phase Coherence Filter

[11] Instead of designing a filter based on the absolute amplitude or the coefficients of the S transform, we design a filter based on the coherence of the phase along the lines of *Schimmel and Paulssen* [1997] and *Schimmel and Gallart* [2007]. The use of phase to weight signals has been proposed The phase coherence in several geophysical arena, such as, for example, receiver functions [*Park and Levin*, 2000], surface waves [*Mellors et al.*, 1998], magnetotellurics [*Egbert and Livelybrook*, 1996], and even in the context on noise correlations [*Prieto and Beroza*, 2008]. In this work, we form a phase coherence filter, f_ϕ by stacking the normalized, complex values of the projections of the DOST

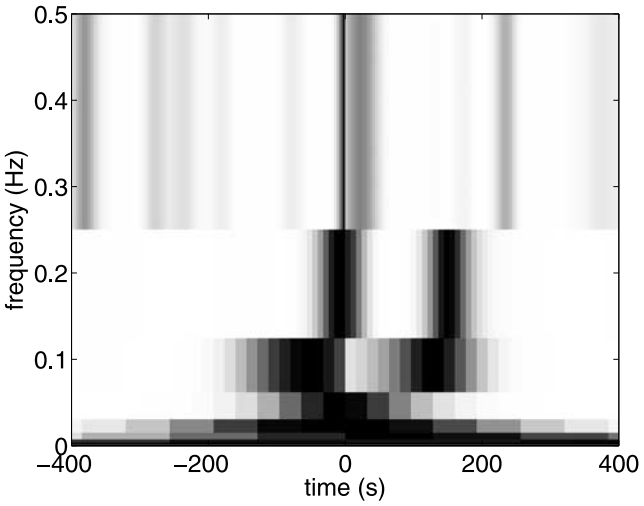

Figure 4. The filter, $f_A(p, \tau)$ (plotted here in terms of frequency and time), for the ZZ cross component displayed in Figure 3. The shading varies from white to black as the amplitude increases from 0 to 1. Persistent, acausal energy in the daily cross correlations, most likely due to the generation of microseismic noise from the tidal interaction of the Pacific Ocean with the California coast [*Stehly et al.*, 2006], is responsible for the notable asymmetry of the filter for the octaves between 0.125 Hz and 0.25 Hz and 0.25 Hz and 0.5 Hz.

basis vectors, and then taking the absolute value of the stack itself:

$$f_\phi(p,\tau) = \text{smoothed}\left|\frac{1}{N_k}\sum_{k=1}^{N_k}\frac{S_{[p,\tau]}(t)c_k(t)dt}{\left|S_{[p,\tau]}(t)c_k(t)dt\right|}\right|^\nu. \qquad (16)$$

This filter is not necessarily maximal for the largest arrivals on the data (unlike the relative amplitude filter discussed in section 3.1), but it is maximal on the most coherent phases. We have the same parameter, ν, to tune the strength of the filter but we use more modest values compared with the amplitude filters in section 3.1: typically, $\nu = 0.5$ achieves a good balance of denoising the trace without distorting the signal. Smoothing these filters, as like in the relative amplitude filters, ameliorates potential problems with the sidelobe energy of individual DOST basis functions. We also divide the input signals by their envelopes, in an effort to deemphasize the amplitude of the direct arrivals.

[12] In Figure 5, we have a color image of the daily correlations between two stations in the network of seismometers deployed on le Piton de la Fournaise volcano on La Réunion Island: each row in the image corresponds to a normalized daily cross correlation between the stations. The data are generally very noisy, and the character of the data changes abruptly in periods of eruptions (i.e., around September 1999; and February, July, and September 2000). We apply the filter to the cross correlations and plot

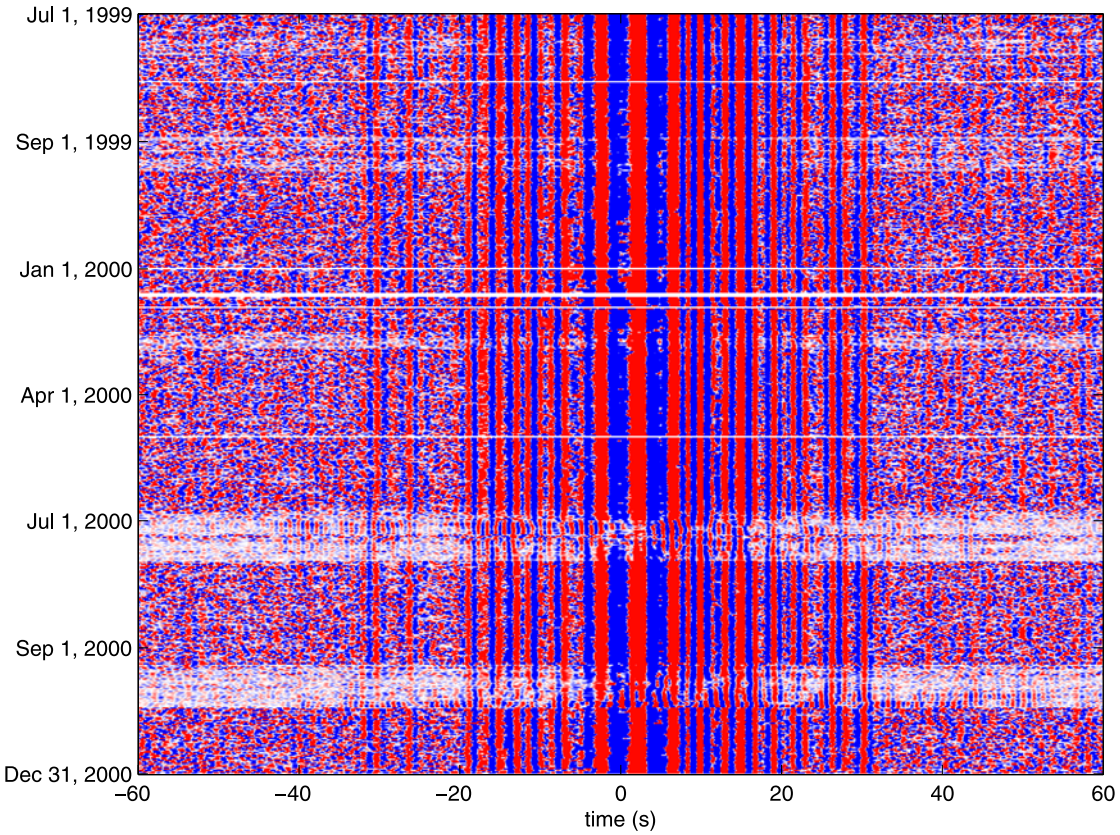

Figure 5. A year and a half of daily cross correlations between two stations (NCR and NTR) monitoring seismicity on the volcano, le Piton de la Fournaise. These data are band-pass-filtered between 0.2 and 0.9 Hz.

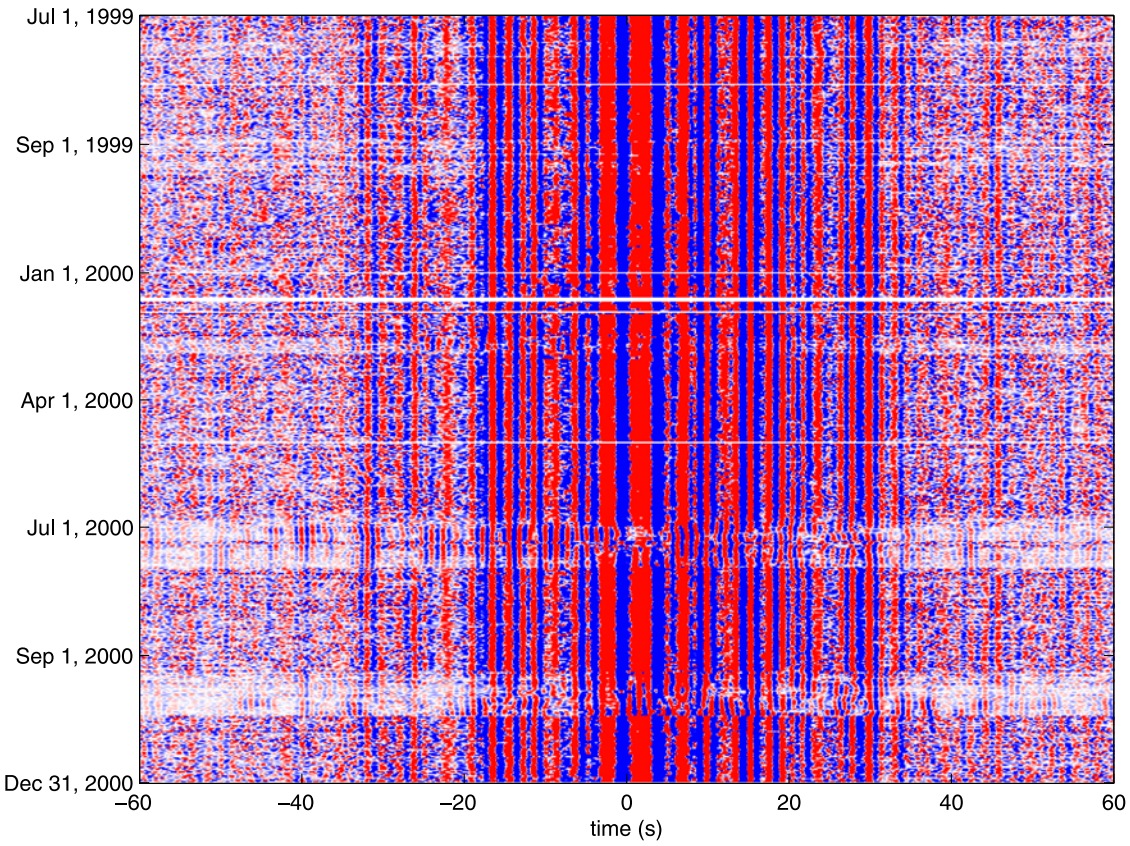

Figure 6. The data plotted in Figure 5 after application of the data adaptive phase coherence filter (and later application of the same band-pass filter as in Figure 5).

the resulting filtered data in Figure 6. The filtering appears to take away most of the noise from Figure 5 and leaves several coherent bands of energy into the latest parts of the coda. In particular, the higher frequency phases beyond 10 s are preserved with no loss of fidelity of the large low-frequency direct waves near zero time. This full-band denoising is a consequence of using a time-frequency architecture to construct our phase coherence filter. To demonstrate that the phase coherence filter produced an improvement to the signal-to-noise ratio of the data that would be unattainable though a purely spectral approach, we plot the spectra of the stacks of the data in Figure 7. The general agreement in the shape of the spectra would indicate that the time-frequency approach we advocate is not sacrificing bandwidth toward gains in signal-to-noise ratios.

4. Improving Traveltime Measurements

[13] We shall apply our relative amplitude filter to a data set of correlation measurements from California. The data

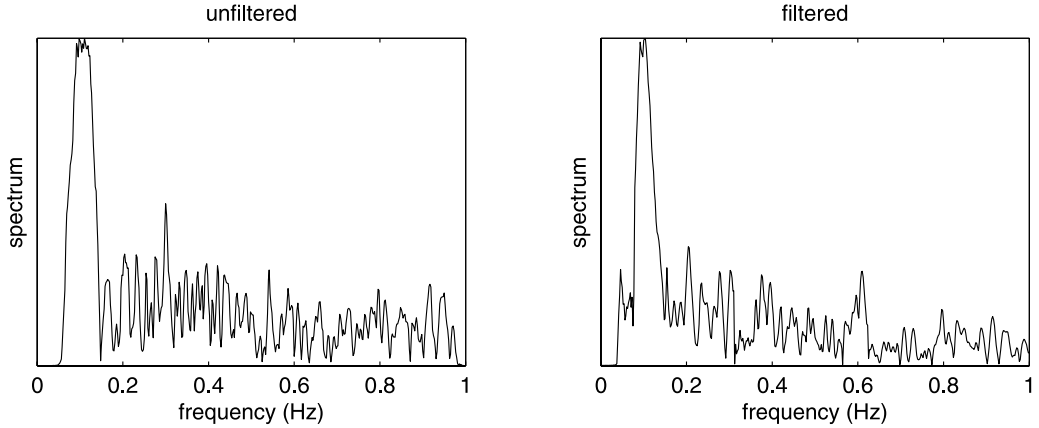

Figure 7. A comparison of the spectra of the total stack of the data plotted in Figures 5 and 6, respectively. Although there are small differences, we note that their general similarity would indicate that the improvement in the signal-to-noise ratio is not at the expense of bandwidth.

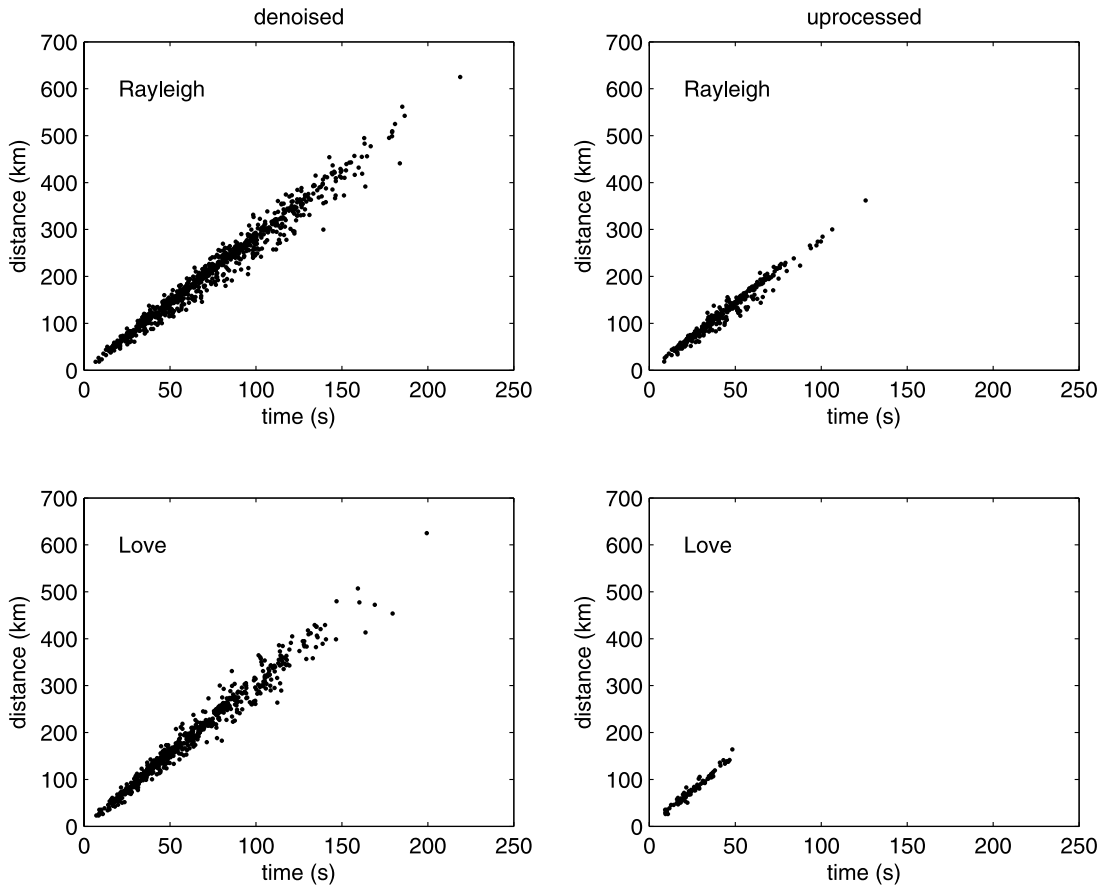

Figure 8. Measured 8s surface wave traveltime versus distance plots. (top left) Denoised Rayleigh wave traveltimes. (top right) Unprocessed Rayleigh wave traveltimes. (bottom left) Denoised Love wave traveltimes. (bottom right) Unprocessed Love wave traveltimes.

are collected for almost 11 months from 60 USArray stations between 11 November 2006 and 30 September 2007 allowing for 1770 station pairs.

4.1. Traveltime Measurement Procedure

[14] There is some preprocessing before the correlations between the stations are calculated; for readers not necessarily interested in all the details of this processing, we would recommend skimming this section to the results. This procedure is largely similar to that described by *Stehly et al.* [2009] First, the data from each station are whitened between 10mHz and 0.4 Hz, then the data are reduced to one-bit correlation functions by dividing them by their absolute value. The whitening helps alleviate the fact that the seismic noise would otherwise be dominated by the micro seismic noise peaks and the one-bit correlations try to minimize the effect of earthquake and other large arrivals on the seismograms. Then we rotate the horizontal components of the data from north and east components to radial and transverse components (relative to the path connecting the station pair) so that we can separate Rayleigh and Love wave energy. The rotated data are divided into individual days and all station pairs are cross correlated. We usually consider only five component cross correlations: the Rayleigh wave will be present on the RR, RZ, ZR, and ZZ components and the Love waves will be present on the TT components. R, T, and Z denoted radial, transverse, and vertical respectively and they appeared paired because to refer to one component from each station (e.g., RZ is the radial component at one station correlated with the vertical component at the other). Because of the first-order decoupling of SH waves from P and SV waves, we expect little to no energy on the cross components TR, TZ, RT, and ZT.

[15] We measure the surface wave dispersion by applying different passbands to these correlations and measuring the traveltimes of the observations. We take advantage of the fact that there may be two observations of the same phase on one component cross correlation to ensure consistency on the data set. In fact, considering the set of cross components RR, RZ, ZR, and ZZ we would have eight possible observations of the Rayleigh wave dispersion. Following the method of *Stehly et al.* [2009], we assess the quality of the measurements. The ''noise'' portion of the cross correlation consists of all data slower than 2 km/s, and the ''signal'' is all the signal faster than that speed. We measure a traveltime for each passband for each trace with a signal-to-noise ratio greater than 7 for both positive and negative times. If we are able to measure a time by finding the maximum of the energy envelope for the causal and acausal parts of a given cross component, and if they fall within 5% of each other, we record that measurement, and then average all such times measured across all the Rayleigh wave cross components for the same station pair. For Love waves, we no longer have the luxury of redundancy of the

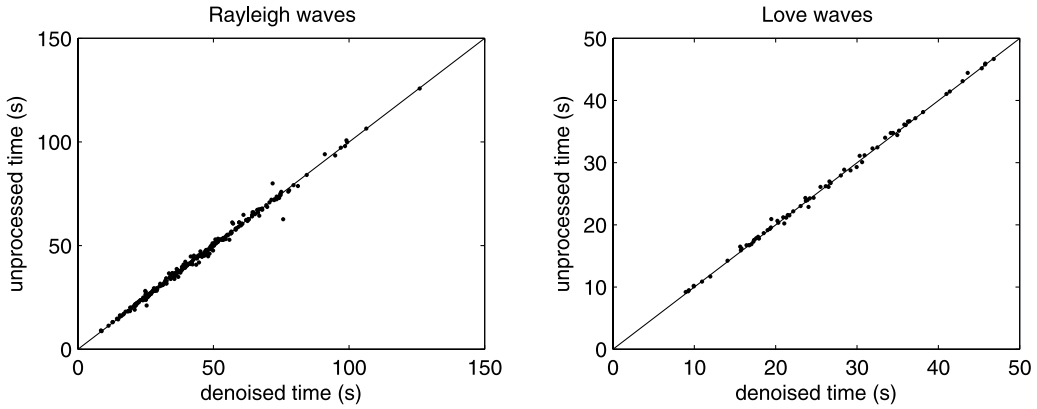

Figure 9. Denoised versus unprocessed 8 s traveltime plots for same station pairs for (left) Rayleigh waves and (right) Love waves.

same phase being recorded on multiple cross components, so we increase of the signal-to-noise ratio cutoff to 10. If this criterion is satisfied on both sides of the signal, a traveltime is measured by averaging the times of the maxima of the energy envelopes on both sides the TT cross component.

4.2. Comparison of Unprocessed and Denoised Data

[16] Figure 8 shows the 8 s Rayleigh and Love wave traveltimes measured across the data set both before (Figure 8, left) and after (Figure 8, right) our denoising routine are applied to the data plotted against the station separation. Figure 8 (top) are Rayleigh wave traveltime while Figure 8 (bottom) are Love wave traveltimes. For the denoised Rayleigh waves, 1168 traveltimes are recorded in contrast to only 285 traveltimes for the unprocessed data. In general, we record fewer Love wave measurements, 758, for the denoised TT cross component and only 82 for the unprocessed data. Notably, without the processing, only the correlations for the closest stations are preserved; by denoising the data, we are able to obtain measurements of surface wave traveltimes across the array. To ensure that our processing is not introducing any artifacts into the traveltime measurements, we plot the accepted Rayleigh and Love wave traveltimes for denoised and unprocessed data against one another in Figure 9. That most of the data fall along a line with a slope of 1 indicates that the processing is not altering the signals in extreme ways to produce faulty measurements. In Table 1, we plot the number of accepted traveltimes in each passband for both the processed and unprocessed Rayleigh and Love wave data. In all cases, more traveltimes are obtained from the denoised data than from the unprocessed cases. The number of accepted data is highest in the 16 s passband for both Rayleigh and Love waves and more data are rejected at the lowest frequencies.

5. Improving Traveltime Delay Measurements as a Volcanic Precursor

5.1. Measuring Phase Delays in Cross Correlations

[17] *Brenguier et al.* [2008b] suggested that time delay measurements on noise cross correlations on the volcano, the Piton de la Fournaise on the island of La Réunion can be used to predict eruptions. The signals used to calculate the time delays reside in the coda of the correlograms, and are subdominant with respect to the main arrival. For this reason, we do not use the relative amplitude filter on these data but instead turn to the phase coherence filter. Although we expect subtle time shifts in the data, indeed this is the observable we wish to resolve, the order of magnitude of the time shifts is generally one part in a thousand, so we would not expect deleterious effects on the phase coherence. To measure the time shifts, we first must define a reference seismogram as the stack of the daily cross correlations. Following the method of *Ratdomopurbo and Poupinet* [1995], the data are first subjected to a 7 s Hanning window, and the slope of the cross spectrum between the daily signal and the stack is computed between 0.2 and 0.9 Hz. From this slope, the time shift between the two signals is calculated in the window; the error is calculated from the coherency of the signal and the width of the band pass and length of the window. We move this Hanning window between −40 s and 40 s in the cross correlations to obtain estimates of time shift with respect to the reference stack for the signal. When these time shifts are averaged over all stations, and a linear relationship is evident between this time shift and the reference time, the slope of the best fitting line can be interpreted as equal to the negative of the average velocity change ($dt/t = -dv/v$) of the medium [*Brenguier et al.*, 2008b]. It is this quantity that has been suggested to be used to predict forthcoming eruptions: it is hypothesized that when this average velocity shift is negative, it reflects the dilatation of the edifice induced by magma pressurization prior to eruptions.

[18] In order to resolve the inflation that precedes the eruption, *Brenguier et al.* [2008b] had to use a 10 day moving

Table 1. Number of Accepted Traveltimes for Denoised and Unprocessed Rayleigh and Love Traveltimes

	Rayleigh		Love	
Period	Denoised	Unprocessed	Denoised	Unprocessed
8 s	878	318	613	86
16 s	1288	674	816	253
24 s	1183	493	564	54
30 s	719	277	67	2
40 s	251	80	0	0

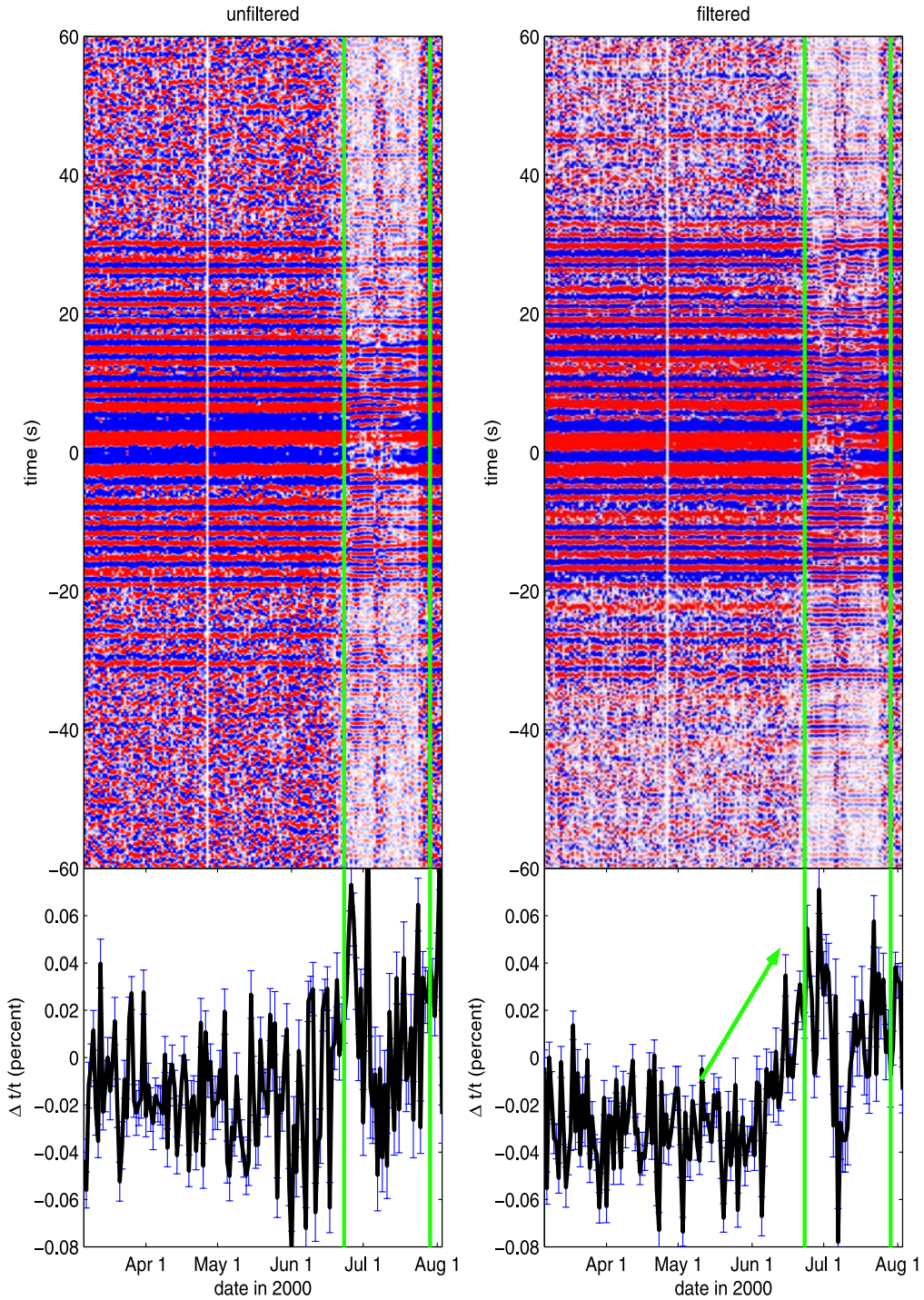

Figure 10. Sections of (top left) unfiltered and (top right) filtered ZZ cross correlations preceding and during an eruption on la Piton de la Fournaise between 23 June and 29 July 2000 (green lines) for the station pair NCR to NTR. Using all station pairs, we can produce plots of relative time shift for (bottom left) the unfiltered data and (bottom right) the filtered data. The green arrow highlights the trend of increasing phase delays before the eruption is much better resolved in the denoised data.

window of data to get a high-fidelity cross correlation. The length of this window impedes the real-time detection of the onset of a potential precursory inflation, so we wish to examine whether application of the phase coherence filter to the data without additional averaging can improve the detection of precursory changes in the volcano.

5.2. Comparing Measurements of Phase Delays Before and After Denoising

[19] In Figure 10, we show how this phase coherence filter improves the temporal resolution of precursory inflation. We examine the period of our data set before and

during an eruption that began on 23 June 2000 and finished on 29 July (marked by the heavy green lines), that same year. Figure 10 is divided into four parts: Figure 10 (left) shows the unfiltered data; Figure 10 (right) shows the filtered data; Figure 10 (top) shows sections of ZZ cross correlations for the station pair, NCR and NTR; and Figure 10 (bottom) shows relative time shifts obtained from averaging time shifts for each individual pair of stations (thick black line) together with the error in measurement. The action of the coherence filter on the data is evident in comparing Figure 10 (top): the preservation of coherent arrivals in the codas of the cross correlations is better in the filtered data. In both cases, the character of the signal around zero time gets much higher frequency during the eruption. However, there appear to be some arrivals that continuously traverse the green line, suggesting that these arrivals are a part of the diffuse part of the Green's function.

[20] Turning our attention to Figure 10 (bottom), showing the relative time shifts averaged over all 13 station pairs in the network, we note that several weeks before the eruption the relative time shifts seem to oscillate around a relatively constant baseline value in both data sets and that an increase in the relative time shift is observed immediately after the eruption. However, what is evident from the filtered data, and not so obvious in the raw data, is that immediately before the eruption, the relative time shifts steadily increase. In the filtered data, this steady increase takes place over a couple of weeks while because of large fluctuations, it is very hard to resolve on the unfiltered data.

6. Conclusions

[21] We have presented a couple of routines for improving the fidelity of noise cross correlations that is based on the discrete orthonormal S transform. These routines are based on the time-frequency transformation facilitated by the DOST basis functions that are both easy to compute and are rapidly evaluated in that they avoid the redundancy inherent in many time-frequency transformations. Furthermore, the time-frequency character of these algorithms allows for simultaneous analysis of the spectral and temporal characteristic of a signal.

[22] By using standard routines to measure Rayleigh and Love wave traveltimes in different passbands for Californian USArray data, we show that by denoising the data, we can recover more traveltime measurements from longer distances. This improvement in path coverage should allow for more constraints to be placed on various geological structures. In addition, our denoising routine will be used in future studies to look for more subdued arrivals on these noise cross correlations to bring further constraints on tomographic studies. We also shown the utility in using these time-frequency, data adaptive filters with the application of volcanic monitoring. We show that changes in the volcano, le Piton de la Fournaise, that precede an eruption are much better resolved after filtering the data. Those concerned with volcanic monitoring would need this type of immediacy, to be able to prepare for the policy decisions, such as issuing evacuation orders.

[23] **Acknowledgments.** This work was funded through the NERIES JRA5 project of the European Community. The manuscript was greatly improved through the comments of G. Prieto, the Associate Editor, and an anonymous reviewer. Discussions with the Equipe Ondes et Structures at LGIT greatly aided the manuscript as well.

References

Brenguier, F., M. Campillo, C. Hadziioannou, N. M. Shapiro, R. M. Nadeau, and E. Larose (2008a), Postseismic relaxation along the San Andreas Fault in the Parkfield area investigated with continuous seismological observations, *Science*, *321*, 1478–1481, doi:10.1126/science.1160943.

Brenguier, F., N. M. Shapiro, M. Campillo, V. Ferrazzini, Z. Duputel, O. Coutant, and A. Nercessian (2008b), Towards forecasting volcanic eruptions using seismic noise, *Nat. Geosci.*, *1*, 126–130, doi:10.1038/ngeo104.

Campillo, M., and A. Paul (2003), Long-range correlations in the diffuse seismic coda, *Science*, *299*, 547–549, doi:10.1126/science.1078551.

Egbert, G. D., and D. W. Livelybrook (1996), Single station magnetotelluric impedance estimation: Coherence weighting and the regression M-estimate, *Geophysics*, *61*, 964–970, doi:10.1190/1.1444045.

Gouédard, P., L. Stehly, F. Brenguier, M. Campillo, Y. ColindeVerdière, E. Larose, L. Margerin, P. Roux, F. J. Sánchez-Sesma, N. M. Shapiro, and R. L. Weaver (2008), Cross-correlation of random fields: Mathematical approach and applications, *Geophys. Prospect.*, *56*, 375–393, doi:10.1111/j.1365-2478.2007.00684.x.

Lobkis, O. I., and R. L. Weaver (2001), On the emergence of the Green's function in the correlations of a diffuse field, *J. Acoust. Soc. Am.*, *110*, 3011–3017, doi:10.1121/1.1417528.

Mellors, R. J., F. L. Vernon, and D. J. Thomson (1998), Detection of dispersive signals using multiple dual-frequency coherence, *Geophys. J. Int.*, *135*, 146–154, doi:10.1046/j.1365-246X.1998.00614.x.

Moschetti, M. P., M. H. Ritzwoller, and N. M. Shapiro (2007), Surface wave tomography of the western United States from ambient seismic noise: Rayleigh wave group velocity maps, *Geochem. Geophys. Geosyst.*, *8*, Q08010, doi:10.1029/2007GC001655.

Nishimura, T. S., S. Tanaka, H. Y. T. Yamawaki, T. Sano, M. Sato, H. Nakahara, N. Uchide, S. Hori, and H. Sato (2005), Temporal changes in seismic velocity of the crust around Iwate volcano, Japan, as inferred from analyses of repeated active seismic experiment data from 1998 to 2003, *Earth Planets Space*, *57*, 491–505.

Park, J., and V. Levin (2000), Receiver functions from multiple taper spectral correlation estimates, *Bull. Seismol. Soc. Am.*, *90*, 1507–1520, doi:10.1785/0119990122.

Pinnegar, C. R., and D. W. Eaton (2003), Application of the S transform to prestack noise attenuation filtering, *J. Geophys. Res.*, *108*(B9), 2422, doi:10.1029/2002JB002258.

Prieto, G. A., and G. C. Beroza (2008), Earthquake ground motion prediction using the ambient seismic field, *Geophys. Res. Lett.*, *35*, L14304, doi:10.1029/2008GL034428.

Ratdomopurbo, A., and G. Poupinet (1995), Monitoring a temporal change of seismic velocity in a volcano: Application to the 1992 eruption of Mt. Merapi (Indonesia), *Geophys. Res. Lett.*, *22*, 775–778, doi:10.1029/95GL00302.

Sabra, K. G., P. Gerstoft, P. Roux, W. A. Kuperman, and M. C. Fehler (2005), Surface wave tomography from microseisms in Southern California, *Geophys. Res. Lett.*, *32*, L14311, doi:10.1029/2005GL023155.

Schimmel, M., and J. Gallart (2007), Frequency-dependent phase coherence for noise suppression in seismic array data, *J. Geophys. Res.*, *112*, B04303, doi:10.1029/2006JB004680.

Schimmel, M., and H. Paulssen (1997), Noise reduction and detection of weak, coherent signals through phase weighted stacks, *Geophys. J. Int.*, *130*, 497–505, doi:10.1111/j.1365-246X.1997.tb05664.x.

Shapiro, N. M., and M. Campillo (2004), Emergence of broadband Rayleigh waves from correlations of the ambient seismic noise, *Geophys. Res. Lett.*, *31*, L07614, doi:10.1029/2004GL019491.

Shapiro, N. M., M. Campillo, L. Stehly, and M. H. Ritzwoller (2005), High-resolution surface wave tomography from ambient seismic noise, *Science*, *307*, 1615–1618, doi:10.1126/science.1108339.

Stehly, L., M. Campillo, and N. Shapiro (2006), A study of the seismic noise from its long-range correlation properties, *J. Geophys. Res.*, *111*, B10306, doi:10.1029/2005JB004237.

Stehly, L., B. Fry, M. Campillo, N. Shapiro, J. Guilbert, L. Boschi, and D. Giardini (2009), Tomography of the Alpine region using seismic ambient noise, *Geophys. J. Int.*, *178*, 338–350, doi:10.1111/j.1365-246X.2009.04132.x.

Stockwell, R. G. (2007), A basis for efficient representation of the S-transform, *Digit. Signal Process.*, *17*, 371–393, doi:10.1016/j.dsp.2006.04.006.

Stockwell, R. G., and G. L. Mansinha (1996), 356 and R. P. Lowe, Localization of the complex spectrum: the S transform, *IEEE Trans. Signal Process.*, *44*, 998–1001, doi:10.1109/78.492555.

Wegler, U., B.-G. Lühr, R. Snieder, and A. Ratdomopurbo (2006), Increase of shear wave velocity before the 1998 eruption of Merapi volcano (Indonesia), *Geophys. Res. Lett.*, *33*, L09303, doi:10.1029/2006GL025928.

A. M. Baig and M. Campillo, Laboratoire de Géophysique Interne et de Tectonophysique, BP 53, F-38041 Grenoble CEDEX 9, France. (abaig@alumni.princeton.edu; Michel.Campillo@obs.ujf-grenoble.fr)

F. Brenguier, Institut de Physique du Globe de Paris, 4 Place Jussieu, F-75252 Paris CEDEX 05, France. (fbrengui@ipgp.jussieu.fr)